NASA TECHNICAL MEMORANDUM

NASA TM X-853

NASA TM X-853

X64 10089

$CODE-2$

A FREE-FLIGHT INVESTIGATION OF THE

HEAT TRANSFER AND AFTERBODY FLOW FIELD

OF AN APOLLO-TYPE CONFIGURATION

AT SPEEDS TO 10,000 FT/SEC

by *Gary T. Chapman and Charles T. Jackson, Jr.*

Ames Research Center

Moffett Field, California

NATIONAL AERONAUTICS AND SPACE ADMINISTRATION • WASHINGTON, D. C. • NOVEMBER 1963

TECHNICAL MEMORANDUM X-853

A FREE-FLIGHT INVESTIGATION OF THE HEAT TRANSFER

AND AFTERBODY FLOW FIELD OF AN APOLLO-TYPE
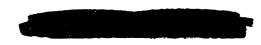
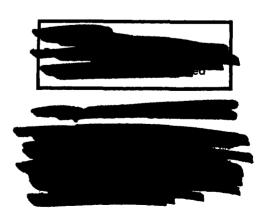CONFIGURATION AT SPEEDS TO 10,000 FT/SEC (U)

By Gary T. Chapman and Charles T. Jackson, Jr.

NASA · Ames Research Center
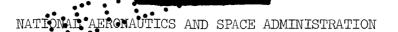Moffett Field, California

NATIONAL AERONAUTICS AND SPACE ADMINISTRATION

NATIONAL AERONAUTICS AND SPACE ADMINISTRATION

TECHNICAL MEMORANDUM X-853

A FREE-FLIGHT INVESTIGATION OF THE HEAT TRANSFER

AND AFTERBODY FLOW FIELD OF AN APOLLO-TYPE

CONFIGURATION AT SPEEDS TO 10,000 FT/SEC*

By Gary T. Chapman and Charles T. Jackson, Jr.

SUMMARY

/0 0 89

Small aluminum models similar to the Apollo Command Capsule were gun-launched at high speeds, allowed to decelerate aerodynamically to a few hundred feet per second, and caught, and their total aerodynamic heat input was measured. Shadowgraph pictures were also taken at various intervals along the flight path for flow-field studies and to determine the velocity-time history of each flight.

The total heat measurements show that, for the trajectories flown, the total heat transfer depends on angle of attack as well as launch velocity. For the small angles of attack, that portion of the initial kinetic energy which goes into heating the model is very small. Furthermore, comparisons with results for other configurations tested in the same manner show that as the total drag coefficient increases, the heat transfer decreases. The total-heat-transfer data were further analyzed, on the basis of the trajectories traversed, to yield instantaneous surface average heat-transfer rates as functions of velocity. These results show that the surface average heat-transfer rate is nearly constant for angles of attack up to that angle at which flow attaches to the afterbody. Above this angle, the average heat-transfer rate increases rapidly with angle of attack.

The shadowgraph studies of afterbody flow indicate large changes in the amount of attached flow with both velocity and angle of attack. Increased velocity reduced the angle of attack required to promote attached flow on the windward side of the afterbody. The separated as well as the attached flow was found to be laminar at all speeds between 1,500 and 6,000 ft/sec. Copy.   AUTHOR

INTRODUCTION

Although considerable effort has been directed toward determining heating loads of Apollo-type vehicles, there still remains a degree of uncertainty as to

the effects of angle of attack on both forebody and afterbody heating load. The latter is related to variations in the extent of afterbody flow separation, which, at present, are not well understood.
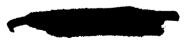
The purpose of this report is twofold: First, to present experimental heating results on a configuration similar to the Apollo vehicle (hereinafter referred to as the blunt capsule), and second, to present experimental results on the shape and nature (i.e., laminar or turbulent) of the free shear layer and the attached flow zones in the afterbody region of the blunt capsule.

SYMBOLS

A_c	maximum cross-sectional area
A_R	reference area for heat transfer
A_w	wetted area
c	specific heat of model material
C_D	total drag coefficient
$C_{D_{av}}$	average drag coefficient defined by equation (9)
d	diameter of model
h	enthalpy
K	constant of proportionality
l	slant length of model afterbody
M	Mach number
m	model mass
n	exponent in equation (4)
Q_{aero}	total aerodynamic heat transfer
$\triangle Q$	energy added to calorimeter
$\dot{q}_{av}$	heat-transfer rate defined by equation (3)
$\dot{q}_l$	local heat-transfer rate
$\dot{q}_{base}$	base heat-transfer rate, referenced to wetted base area

R_∞ Reynolds number based on free-stream properties, $\dfrac{\rho_\infty V_\infty d}{\mu_\infty}$

R_{ns} Reynolds number based on properties behind a normal shock, $\dfrac{\rho_{ns} V_{ns} d}{\mu_{ns}}$

r reference radius of curvature

St Stanton number

s station of flow reattachment on windward side of afterbody

T_c temperature of the calorimeter

T_m temperature of the model

t time

V velocity

x distance along the flight path

ρ density of the air

μ coefficient of viscosity

α angle of attack

α_0 initial condition for normalizing angle of attack

ξ dynamic-stability parameter

λ wave length of pitching oscillation

Subscripts

h portion of trajectory during which heat is being added to model

i conditions prior to launch

L launch conditions

ns conditions behind normal shock

RMS root mean square

st stagnation conditions

w wall (model surface) conditions

∞ free-stream conditions

3

TEST PROCEDURE

Test Apparatus

The experimental heat-transfer data for this report were obtained by measuring, in a calorimeter, the total heating of a model fired through a long ballistic range (see ref. 1). This method is illustrated in figure 1. Here a model launched from a gun is shown traveling through a ballistic range where shadowgraph pictures are taken. The model scale, model material, air density, and range length are selected so that the model decelerates to a few hundred feet per second before entering the catcher. It is further decelerated to zero forward velocity as it pierces sheets of paper. The model then falls through a paper funnel into a calorimeter where the total heat input is measured. A sectional drawing of the calorimeter and a typical output record are shown as inserts in figure 1. A detailed description of the calorimeter and how it works is given in reference 1.

Analysis of the total heat transfer of several different shots with different launch velocities yields the instantaneous surface average heat-transfer rate as a function of velocity.

Description of Model

A drawing of the blunt capsule is shown in figure 2(a). The models were made in one piece of 7075T6 aluminum. The model material and diameter were selected so that the model would decelerate from launch speed to less than 500 feet per second in the length of the ballistic range. A photograph of a typical model and sabot is shown in figure 2(b).
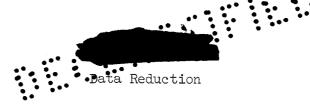
Test Conditions

All of the tests were conducted at sea-level atmospheric conditions. The values of the important test conditions are listed in table I. The free-stream Reynolds number varied directly with the free-stream velocity:

$$R_\infty = 6.25 \ dV_\infty \times 10^3 \tag{1}$$

where V_∞ is the flight velocity, in feet per second, and d is the body diameter, in feet. Another form of the Reynolds number, which is useful in heat-transfer correlations, is based on gas properties behind the normal shock and the body diameter. This Reynolds number, R_{ns}, is nearly constant over that portion of the trajectory during which the major portion of the heating occurs and is approximately 0.20 million.

Data Reduction

Heat-transfer reduction.- The calorimeter responds to the difference between the model mean temperature and that of the calorimeter. This difference includes the effects of heating during flight and the difference existing just prior to the test, so that

$$Q_{aero} = \underbrace{\Delta Q}_{\substack{\text{heat added to} \\ \text{the calorimeter}}} + \underbrace{mc(T_c - T_m)_i}_{\substack{}} \qquad (2)$$

correction due to possible differences
in initial temperature of model and
calorimeter

In the derivation of equation (2) there are assumed to be no extraneous heat sources or sinks; the validity of this assumption is discussed in detail in reference 1. The possible errors introduced will be outlined in the section on error analysis.

The values of total aerodynamic heat transfer, Q_{aero}, at different launch velocities, may be analyzed to yield instantaneous surface-average heating rates, as described in reference 1. The instantaneous surface-average heating rate, $\dot{q}_{av}$, is defined as

$$\dot{q}_{av} = \frac{1}{A_R} \int_{A_W} \dot{q}_l dA_W \qquad (3)$$

where $\dot{q}_l$ is the heat-transfer rate at a point on the surface, A_R is the reference area for heat transfer, and A_W is the wetted area of the body. A functional relationship between $\dot{q}_{av}$, free-stream density, and velocity is assumed:

$$\dot{q}_{av} = K \sqrt{\frac{\rho_\infty}{r}} V_\infty{}^n \qquad (4)$$

where ρ_∞ is the free-stream density, r is a reference radius (e.g., radius of curvature at the stagnation point), V_∞ is the flight speed, and K and n are constants to be determined.

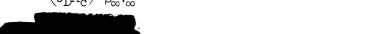The total aerodynamic heat transfer to a model over a given trajectory can be expressed as

$$Q_{aero} = A_R \int_0^t \dot{q}_{av} dt \qquad (5)$$

where t is the time of flight.

From the equation of rectilinear motion, we obtain

$$dt = \left(\frac{-2m}{C_D A_c}\right) \frac{dV}{\rho_\infty V_\infty{}^2} \qquad (6)$$

5

Equations (4), (5), and (6) may be combined and integrated for a constant drag coefficient to yield

$$Q_{aero} = \frac{K2mA_R}{\sqrt{\rho_\infty r} \; A_c C_D} \; \frac{V_L^{n-1} - V_{catch}^{n-1}}{n - 1} \tag{7}$$

Since the launch and catch velocities and drag coefficient are known from chronograph records and shadowgraphs, n and K may be selected to obtain a best fit to the experimental values of Q_{aero}.

The analysis described above works very well if both K and n are constant or very nearly constant over the trajectory; however, this is true only for the case of near-zero angle of attack or where the heating rate is independent of the angle of attack. The blunt capsule configuration does not meet these requirements. It was thought, however, that, for a fixed value of RMS angle of attack, defined by

$$\alpha_{RMS}^2 = \frac{1}{x_h} \int_0^{x_h} \alpha^2 dx \tag{8}$$

where x_h is that portion of the flight during which heat is being taken into the model, the values of K and n would be nearly constant; that is, $K = K(\alpha_{RMS})$ and $n = n(\alpha_{RMS})$. Furthermore, the drag coefficient for the blunt capsule is a function of angle of attack. Therefore the value of C_D used in equation (7) is the average C_D, defined by equation (9) over the angle-of-attack range corresponding to α_{RMS}:

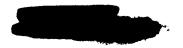$$C_{D_{av}} = \frac{\int_0^{x_h} C_D dx}{x_h} \tag{9}$$

It is realized that the above-outlined technique for handling the effects of angle of attack is approximate.

Determination of launch velocity and drag.- The launch velocity (i.e., velocity at the muzzle of the gun) was deduced from shadowgraph and chronograph records, from stations located 14 to 20 feet from the gun muzzle by extrapolating these measurements back to the gun muzzle. This extrapolation was based on experimental drag coefficients and the equation of motion along the flight path, with distance instead of time as the independent variable; that is,

$$\frac{dV}{dx} = \frac{-C_D A_c}{2m} \rho_\infty V_\infty \tag{10}$$

The drag data presented in the report were deduced from the velocity history obtained from the first seven shadowgraph stations by use of equation (10). This was done by assuming that, over a short distance, the drag coefficient, C_D, is constant. Equation (10) can then be integrated directly to yield

$$\ln V = \frac{-A_c \rho_\infty}{2m} C_D x + constant \tag{11}$$

6

The drag coefficient may be found by plotting the logarithm of the measured velocity, V, versus x. The local slope of this curve is proportional to C_D and the constants of proportionality are known. Extension of the curve (which is in general a nearly straight line) back to the station of the gun muzzle gives the velocity of the model at launch.

Angle of attack.- A study of the data of the present investigation shows that heat transfer is a strong function of the pitching amplitude; therefore, it was necessary to determine the pitching history of each model.

By a strange quirk of fate the relationship between the oscillation wave length and the spacing between shadowgraph stations precluded direct determination of pitching history - that is, $\lambda = 3.75$ feet[1] and the station spacing was 7 feet. However, it was possible to determine the root-mean-square (RMS) angle of attack by use of the relationship between the RMS angle of attack and the measured drag coefficient from reference 2, which is shown in figure 3. From a measurement of the local slope of the natural logarithm of V versus x curve at any desired point along the trajectory, the drag coefficient was obtained, and the corresponding RMS angle of attack read from figure 3. This procedure assumes that the drag coefficient for this configuration is independent of Mach number, at least for Mach numbers greater than about 2. This assumption is believed to be valid because of the known insensitivity of C_D to Mach number in the high supersonic speed range for this class of configurations. The RMS angles of attack obtained in this manner are thought to be accurate to within $\pm 3^\circ$. The values of RMS angle of attack quoted in this report for the blunt capsule configuration are for a position 18 to 22 feet from the gun muzzle, hereinafter referred to as station 1.
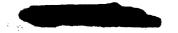
Error Analysis

The accuracy of the total aerodynamic heat-transfer measurements depends on recording equipment and the elimination of extraneous sources and sinks of heat. The estimated accuracies for total aerodynamic heating are presented below for three different launch velocities.

	Error range, percent	Velocity, ft/sec
Total aerodynamic heating, Q_{aero}	+13 to -20	5,000
	+8 to -15	7,000
	+6 to -13	10,000

A detailed discussion of the sources of error can be found in reference 1. The errors listed above are about 5 percent higher than those quoted in reference 1, because one of the protective devices used to shield the flat-based models against propellant gases was not adaptable to the blunt capsule model.

---

[1]The wave length of these oscillations was estimated from the model properties and test conditions and was verified through the use of three temporary shadowgraph stations inserted between two permanent stations.

The inaccuracies in the average heating rates, $\dot{q}_{av}$, are difficult to ascertain because the integral procedure used in obtaining the results makes use of an assumed functional dependence, equation (4). It is thought, however, that the inaccuracy can be as large or larger than the errors in the total aerodynamic heating data. In reference 1 it was shown that the maximum error in $\dot{q}_{av}$ was approximately equal to the maximum error in the total heat measurement Q_{aero} for a hemisphere.

The estimated accuracy of other pertinent quantities is listed below.

Measured drag coefficient, C_D	±1 percent
Launch velocity, V_L	±1 percent
RMS angle of attack, α_{RMS}	±3°
Amount of windward meridian on afterbody covered by attached flow, $(l - s)/l$	±0.10

RESULTS AND DISCUSSION
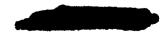
Heat-Transfer Data

Total heat transfer.- The total heat, Q_{aero}, transferred to the blunt capsules is shown in figure 4 as a function of launch velocity. These results are also given in table I. The RMS angle of attack determined at station 1 is indicated in brackets beside each test point. The RMS angle of attack can be seen to have considerable effect on the total heat transferred to the blunt capsule. This will be discussed later in the report. The two lines in this figure are thought to represent approximately the total heat transfer at RMS angles of attack of 0° and 16°.

It should be noted that the results presented in figure 9 of reference 1 demonstrate that the spread of the experimental points in figure 4 is not due to experimental scatter.

Fraction of the kinetic energy appearing as heat transfer.- A figure of merit useful in studying heating loads to reentry vehicles is the fraction of the initial kinetic energy which appears as heat transferred to the vehicle. The total aerodynamic heat transfer divided by the kinetic energy at launch is shown plotted in figure 5(a) as a function of velocity. Note that less than one percent of the initial kinetic energy appears as heat transferred to the model, and furthermore that this fraction is nearly independent of velocity but is dependent on angle of attack.

Similar results for a hemisphere and 60° blunted cone (ref. 1) are also shown on this figure. In comparing the different configurations, it is interesting to note that for the speed range covered and for small angles of attack, the smaller the drag coefficient the larger the fraction of the initial kinetic energy which appears as heat transfer. These same basic results, normalized by the square root of the Reynolds number based on flow properties behind the

normal shock, are shown in figure 5(b). Plotted in this manner the data are more easily used to calculate heating loads at other test conditions, and show the same basic trends as figure 5(a).

Heat-transfer rates as a function of velocity.- Upon applying the data reduction method described earlier to the total heat-transfer results and using the drag coefficients to be presented later, we obtain heat-transfer rates in the form

$$\dot{q}_{av} = K \sqrt{\frac{\rho_{\infty}}{r}} \, V_{\infty}^{n} \tag{4}$$

where the values of K and n determined from the data of the present tests are 1.95×10^{-7} and 2.7, respectively. The test results in the form of equation (4) are plotted in figure 6, referenced to the maximum cross-sectional area of the body, as a function of velocity for 0° angle of attack. When considered in the context of equation (4), the slope of the curve in figure 6 is equal to the exponent n. The larger the value of n, the faster the heating rate increases with velocity. The value of n for the blunt capsule, determined from the present tests, 2.7, is different from the 3 to 3.2 obtained from tests on the other configurations (ref. 1) and from theoretical results. This difference may be due to changes in afterbody heating resulting from flow-field changes with velocity or it may reflect an inaccurate definition of the line slopes in figure 4.
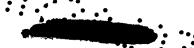
Dimensionless heat-transfer parameter.- The heat-transfer rates were reduced to dimensionless form as follows. The average Stanton number, St, is defined as

$$St = \frac{\dot{q}_{av}}{(h_{st} - h_{w})\rho_{ns}V_{ns}} \tag{12}$$

where the subscript, ns, refers to conditions behind the normal shock, and h_{st} and h_{w} are the stagnation and wall enthalpies, respectively. For the present tests h_{w} was taken as the wall enthalpy prior to launch. This was found to be a satisfactory assumption for that portion of the trajectory during which the major portion of the heating was taking place (ref. 1).

The product of Stanton number, based on the $\dot{q}_{av}$ curve of figure 6 and on maximum cross-sectional area, and the square root of the Reynolds number, based on properties behind the normal shock, is plotted in figure 7 as a function of stagnation enthalpy for the blunt capsule at zero angle of attack. It can be seen that $St\sqrt{R_{ns}}$ is relatively insensitive to changing stagnation enthalpy. Also shown are the results for a hemisphere and a 60° blunted cone. Note that the results for these configurations, having wide variations in local heating rates and large differences in base area, are closely grouped when plotted in this manner.

Effect of Angle of Attack and Afterbody
Heating on the Blunt Capsule

In discussing the effect of angle of attack on the heat transfer to the blunt capsule, one should keep in mind that the data were obtained from an oscillating model traversing a decelerating trajectory. A normalized angle-of-attack history of one of the models is shown in figure 8. The method described in reference 3 was used to calculate this angle-of-attack history. A measured wave length of 3-3/4 feet and a value of the dynamic-stability parameter, ξ, of 1.0 were used in this calculation.[2] (This value of ξ was obtained from ref. 2. An analysis of the present data indicates that this value may be slightly high for the conditions of the present tests.) Note that the pitching oscillation is diverging slightly, primarily as a result of decreasing dynamic pressure as the model decelerates. The case presented in figure 8 is thought to be the most divergent oscillation encountered in the present tests. The fraction of the total heat input to the model as a function of the distance traveled is also presented in this figure. At a distance of 20 feet from the gun muzzle, 80 percent of the heating has already occurred and the maximum pitching amplitude has increased by 30 percent from its initial value. This shows that although the oscillations are divergent, the amplitude is nearly constant during the period of high heat transfer. Furthermore, because of this divergent character, the value of α_{RMS} (which is measured at station 1) is different from the RMS angle of attack over the distance interval from the gun muzzle to station 1. However, these two values of RMS angle of attack are related by
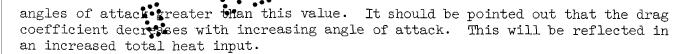
$$\frac{\alpha_{RMS}\Big|_{0-20}}{\alpha_{RMS}\Big|_{stal}} = \frac{\sqrt{\frac{1}{20}\int_0^{20}\alpha^2 dx}}{\sqrt{\frac{1}{\lambda}\int_{20-(\lambda/2)}^{20+(\lambda/2)}\alpha^2 dx}} \tag{13}$$

where λ is the wave length of the pitching oscillation. This ratio is 0.88 for the pitching oscillation shown in figure 8. The integral in the numerator of equation (13) is not available from experimental information but the ratio defined by equation (13) is, in general, within about 10 percent of unity. The RMS angle of attack determined at station 1 was used for gaging the effects of angle of attack on heat transfer.

<u>Effects of angle of attack on the total heat transfer</u>.- The total heat transfer plotted versus RMS angle of attack for the blunt capsule at two different launch velocities is shown in figure 9. These curves were constructed from extrapolated and interpolated data from figure 4, since there was not a complete range of α_{RMS} in the data at any one velocity. Also shown is a line at $\alpha_{RMS} = 18.74°$ which corresponds to the RMS angle of attack below which the afterbody is always in the shadow, so to speak, of the front face. It appears, particularly for the lower speed, that the heating increases significantly for

---

[2]The dynamic-stability parameter referred to is the combined parameter defined in reference 3, which includes the effects of deceleration, model plunging, and conventional damping in pitch on the envelope of the pitching oscillations.

10

angles of attack greater than this value. It should be pointed out that the drag coefficient decreases with increasing angle of attack. This will be reflected in an increased total heat input.

Effects of angle of attack on the heat-transfer rates.- If these results are analyzed to obtain $\dot{q}_{av}$ with the restriction that the value of n is constant, we obtain the results shown in figure 10, namely, the ratio of the heating rate to the heating rate at $\alpha = 0$, $\dot{q}_{av}/\dot{q}_{av_{\alpha=0}}$, versus the RMS angle of attack. It is now evident more pronouncedly than in figure 9 (because of the influence of C_D in eq. (7)) that as soon as the angle of attack is sufficiently large to make the windward afterbody surface a compression surface, the heat-transfer rate increases significantly. The curve indicates that the heat-transfer rate at the higher speed starts to increase at a lower angle of attack than does that at the lower speed. This would appear to indicate that attachment of the flow to the afterbody is occurring at a lower angle of attack at the higher speed. This indeed is what is observed in shadowgraph pictures, as will be discussed later.

Afterbody heating.- Crude estimates of the base heating were obtained by subtracting theoretical front-face heating rate (calculations based on refs. 4, 5, and 6) from the heating rate for the entire blunt capsule.

The base heat-transfer estimates obtained in this manner are not very accurate because they involve the subtraction of two numbers whose difference is as large as the possible inaccuracies in the original two numbers. However, it was thought that these results were still of some interest, because there are very few base heat-transfer results available and those available frequently include the effects of sting interference.

The base heat-transfer rates (referenced to wetted afterbody area which is 2 times the cross-sectional area) for $\alpha = 0$, divided by the theoretical stagnation-point heating rate (ref. 4), are plotted in figure 11. The solid line indicates the values as calculated; the shaded area represents the maximum possible combinations of error. It should be noted that because of the large base area, these results imply extremely large amounts of base heating. This appears to be too high, indicating that the inaccuracies described earlier tend to be all additive. Also shown are some results for afterbody heating of the Mercury capsule (ref. 7). It can be seen that the present results fall considerably above those of reference 7. The extreme increase in base heating with decreasing velocity does not appear to be realistic and probably reflects the larger experimental errors at the lower speeds.

Base Flow

It is possible to study certain features of the afterbody flow field as affected by speed (or Reynolds number) and angle of attack because of the large number of shadowgraph pictures of the blunt capsule taken during the heat-transfer tests (e.g., figs. 12(a), (b), and (c)). The observed features are summarized in figure 13. The condition of the afterbody flow pattern on the windward side, that is, attached or separated, is indicated by solid and open

symbols, respectively, for various angles of attack and velocities. (On the sheltered side, the flow was always separated.) The number beside each solid symbol indicates the percentage of the windward meridian covered by attached flow. The two shaded lines divide the data according to separated, partially attached, and fully attached flow regimes. It can be seen that these two lines appear to join at about 7,000 feet per second; what happens above this velocity is not known, but it is thought that the flow may be fully attached at the Reynolds numbers shown for small angles of attack.

Also shown on this figure are a series of dashed lines which separate regions of laminar, transitional, and turbulent flow. In the region labeled turbulent flow, the boundary-layer flow is turbulent everywhere downstream of the model shoulder. Note that this region is confined to the low speeds where the Reynolds numbers were very low, contrary to what might have been expected. There are several possible reasons for this; however, the one that appears to be most applicable is that the flight velocity is near sonic speed and there are many small normal shock waves in the flow field. This induces large disturbances into the free shear layer causing transition. Two regions of transitional flow are shown. In these, transition occurs either in the free shear layer or upon reattachment. The laminar region at intermediate speeds is characterized by laminar flow all the way to the recompression shock waves at the minimum wake diameter station behind the model. The lack of shadowgraphs at the higher speeds prevented analysis of the flow above 8,000 feet per second.

From this figure it can be seen that attachment occurs at lower angles of attack at higher speeds. Since attached flow will, it is suspected, yield greater base heating than separated flow, the area covered by attached flow was studied in more detail.

Attachment pattern.- Some idea of the attachment pattern was obtained from a survey of many shadowgraphs. The results of this survey are shown in figure 14. The afterbody of the blunt capsule configuration is shown "developed" onto a flat surface. Approximate lines of flow attachment for two different angles of attack are indicated by lines through the symbols. The entire region within a line is a region of attached flow. The percentage of the wetted base area covered by attached flow is plotted versus angle of attack in figure 15. It can be seen that the fraction of the base area covered by attached flow increases very rapidly with angle of attack at a nominal speed of 3,300 feet per second.

Drag Data

Knowledge of the drag history was essential to analysis of the experimental total-heat-transfer data. The drag results for the blunt capsule are shown in figure 16. A separate set of data is shown for each test because of the sensitivity of the drag coefficient to variations in angle of attack; the small pitching amplitudes correlate with the highest drag. In fact, figure 3 can be used to assign RMS angles of attack to each run at all distances from the gun for which the Mach number is greater than 2. The data points at Mach number equal to 5.5 in this figure were obtained by extrapolating the drag data back along the flight

path to a point where $M = 5.5$. A further point of interest is that the tumbling model (run 44) has a drag coefficient nearly equal to that of a sphere (C_D for a sphere varies from 0.91 to 1.00 over this speed range).
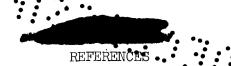
Summary of Experimental Results

Experimental heat-transfer results were obtained on a configuration similar to the Apollo vehicle. The following are some of the results:

1. It was found that the portion of the initial kinetic energy which appears as heat transferred to the blunt capsule is small and, furthermore, when compared to other configurations, that configuration having the largest drag has the least amount of heating.

2. The effect of stagnation-point enthalpy on the heat-transfer parameter, $St \sqrt{R_{ns}}$, was small.

3. Heat transfer to the blunt capsule increased with increasing angle of attack. This resulted from both decreased drag and increased amount of attached flow on the afterbody. The latter effect is particularly important at angles of attack greater than the afterbody half angle.

4. There was considerable heat transfer to the base of the blunt capsule; however, the experimental accuracy with which the base heat-transfer rates could be obtained from present measurements was poor.
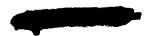
In the process of obtaining the heat-transfer data, many shadowgraphs were taken. A detailed study of the shadowgraphs of the blunt capsule revealed two interesting features in the flow around the afterbody:

1. Flow attachment to the windward side of the afterbody of the blunt capsule was found to occur at progressively lower angles of attack with increasing speed; the windward side experienced fully attached flow at less than 10° angle of attack for the test Reynolds numbers at a speed of 7,000 feet per second.

2. The afterbody area covered by attached flow at the lower speeds was found to increase very rapidly with angle of attack for angles above 17°.

Ames Research Center
National Aeronautics and Space Administration
Moffett Field, Calif., July 19, 1963

REFERENCES

1. Chapman, Gary T., and Jackson, Charles T., Jr.: Free-Flight Investigation of the Heat Transfer to Two Blunt Bodies of Revolution at Speeds to 11,000 ft/sec Using a Catcher-Calorimeter. NASA TN D-1890, 1963.

2. Intrieri, Peter F.: Effects of Transverse Center-of-Gravity Displacement, Afterbody Geometry, and Front-Face Curvature on the Aerodynamic Character- istics of Mercury-Type Models at a Mach Number of 5.5. NASA TM X-569, 1961.

3. Seiff, Alvin, Sommer, Simon C., and Canning, Thomas N.: Some Experiments at High Supersonic Speeds on the Aerodynamic and Boundary-Layer Transition Characteristics of High-Drag Bodies of Revolution. NACA RM A56I05, 1957.

4. Fay, J. A., and Riddell, F. R.: Theory of Stagnation Point Heat Transfer in Dissociated Air. Jour. Aero. Sci., vol. 25, no. 2, Feb. 1958, pp. 73-85, 121.

5. Kemp, Nelson H., Rose, Peter H., and Detra, Ralph W.: Laminar Heat Transfer Around Blunt Bodies in Dissociated Air. Jour. Aero/Space Sci., vol. 26, no. 7, July 1959, pp. 421-430.

6. Boison, J. Christopher, and Curtiss, Howard A.: An Experimental Investiga- tion of Blunt Body Stagnation Point Velocity Gradient. ARS Jour., vol. 29, no. 2, Feb. 1959, pp. 130-135.

7. Reller, John O., Jr., and Seegmiller, H. Lee: Pressure and Heat-Transfer Measurements on a Mercury Capsule Model. NASA TM X-647, 1962.

8. Sammonds, Robert I., and Dickey, Robert R.: Effectiveness of Several Control Arrangements on a Mercury-Type Capsule. NASA TM X-579, 1961.

TABLE I.- TEST CONDITIONS AND RESULTS FOR BLUNT CAPSULE

	Test conditions				Test results			
Run	Ambient pressure, psia	Ambient temp., °F	Model temp. prior to launch, °F	Model weight, grams	V_L, ft/sec	$Q_{aero} \times 10^3$, Btu	No. sheets penetrated	α_{RMS}, deg
326	14.78	63.9	72.0	0.2361	9,915	4.58	33	11.8
403	14.83	62.8	67.2	.2262	8,540	5.05	48[a]	30.4
404	14.76	62.9	68.4	.2254	7,720	3.77	48[a]	24.2
405	14.81	63.6	62.1	.2264	9,080	3.71	41	17.5
438	14.84	66.7	61.9	.2293	5,540	1.73	40	16.3
443	14.75	65.6	60.5	.2279	5,520	3.43	45	Tumbling
459	14.89	62.1	57.7	.2299	5,800	1.70	29	3
460	14.71	63.7	60.1	.2313	7,170	3.40	46[a]	26.8
475	14.88	53.6	54.0	.2284	5,740	1.98	39	23.5
476	14.88	57.7	54.9	.2292	5,550	3.05	47[a]	30.7

[a]Model penetrated all available paper and hit rubber backstop before falling into calorimeter.

16
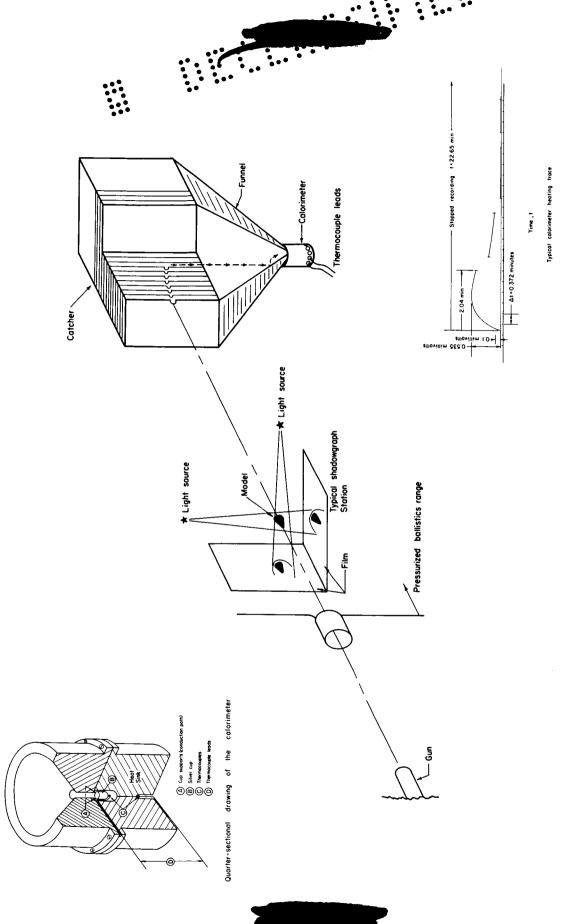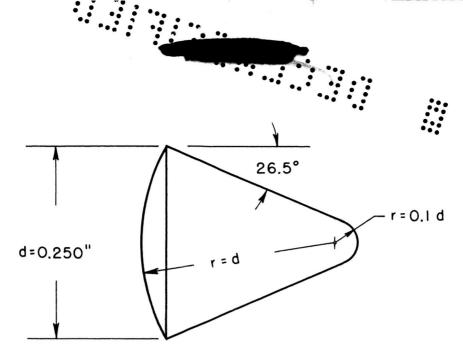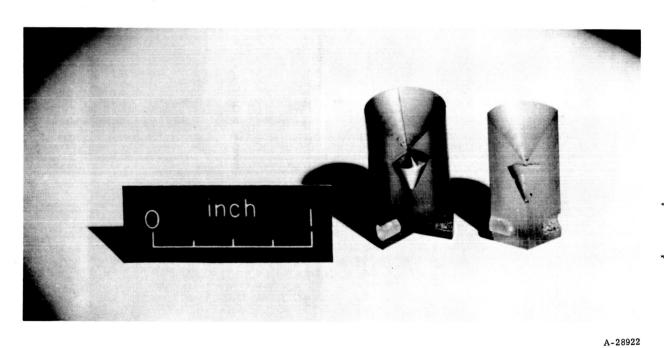
Figure 1.- Schematic drawing of test setup with inserts showing a quarter section of the calorimeter and a typical calorimeter record.

26.5°

r = 0.1 d

d = 0.250"

r = d

(a) Drawing of the blunt capsule.

inch

A-28922
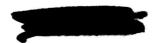
(b) Photograph of the blunt capsule

Figure 2.- Test configuration.
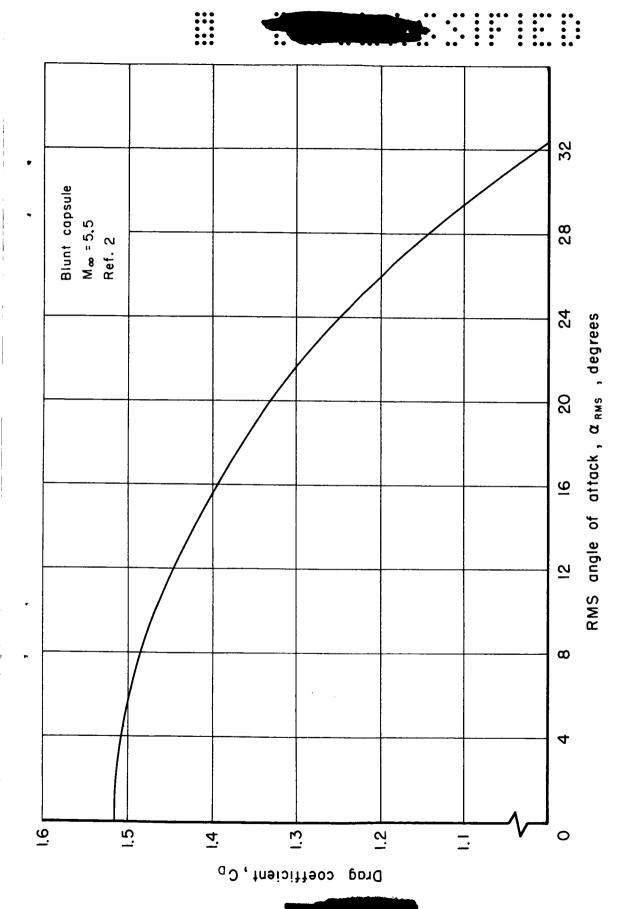
Figure 3.- Drag coefficient of the blunt capsule versus RMS angle of attack.
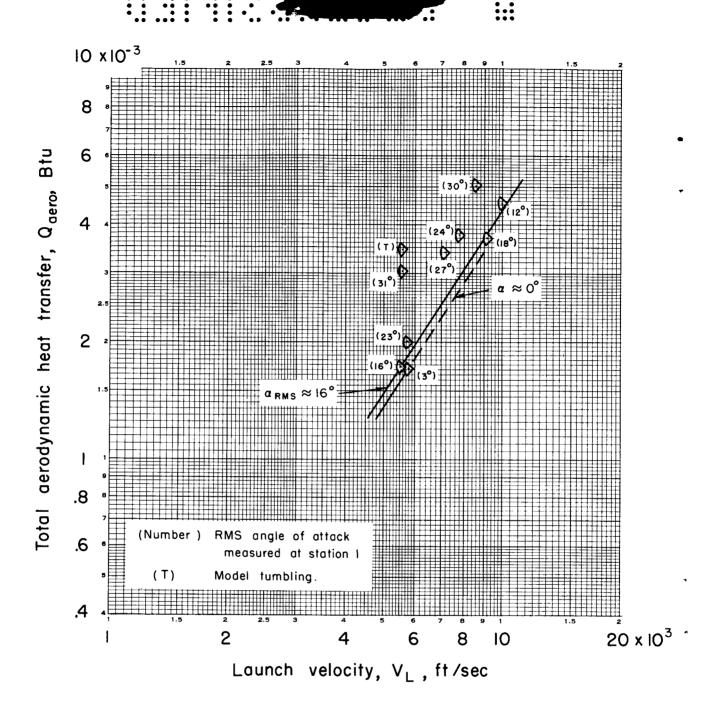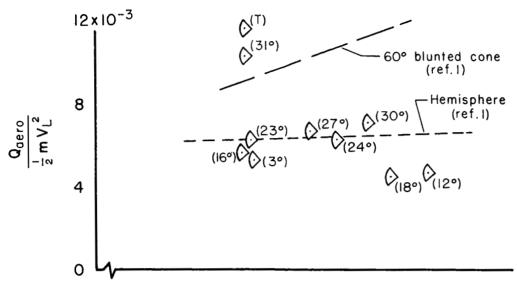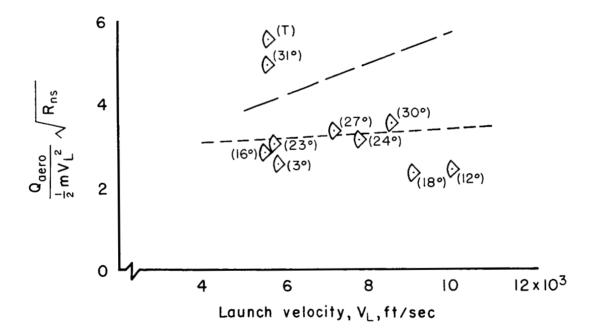
Figure 4.- Total aerodynamic heat transferred to the blunt capsule.

(a) Fraction of the initial kinetic energy.

(b) Normalized fraction of the initial kinetic energy.

Figure 5.- Fraction of the initial kinetic energy resulting in heating of the blunt capsule.
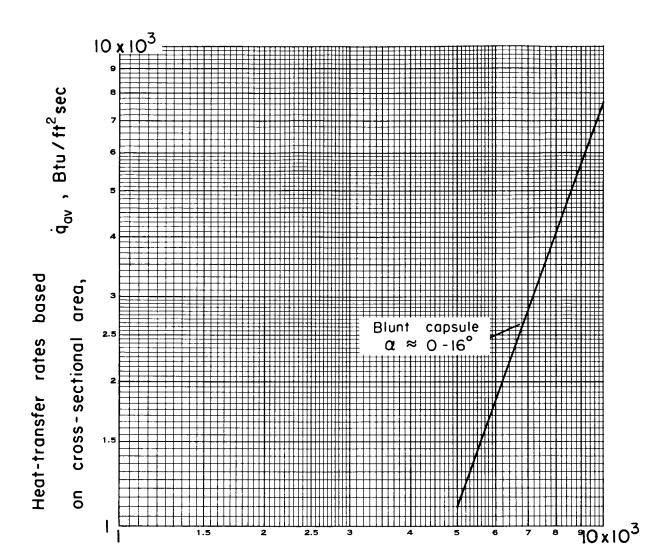
Figure 6.- Heat-transfer rates based on cross-sectional area.
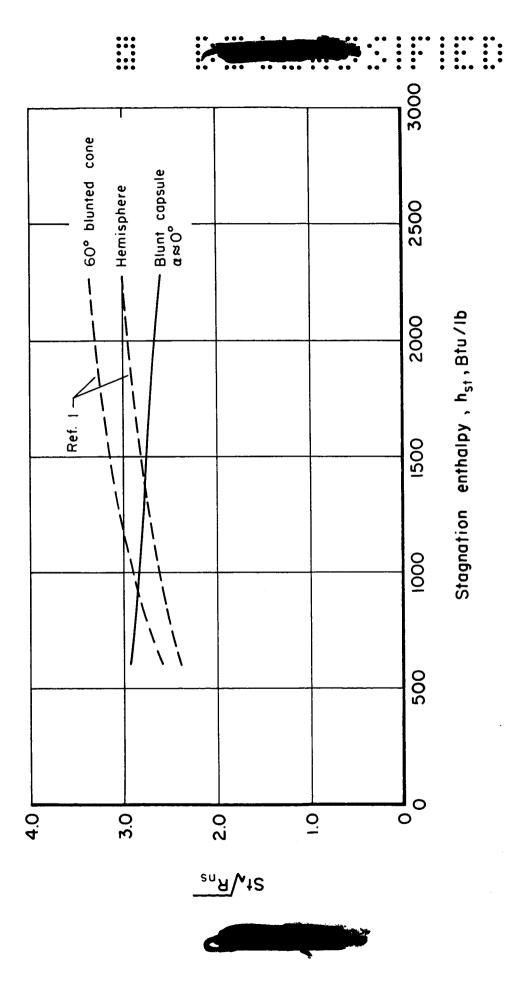
Figure 7.- The effect of stagnation-point enthalpy on the heat-transfer parameter based on cross-sectional area.
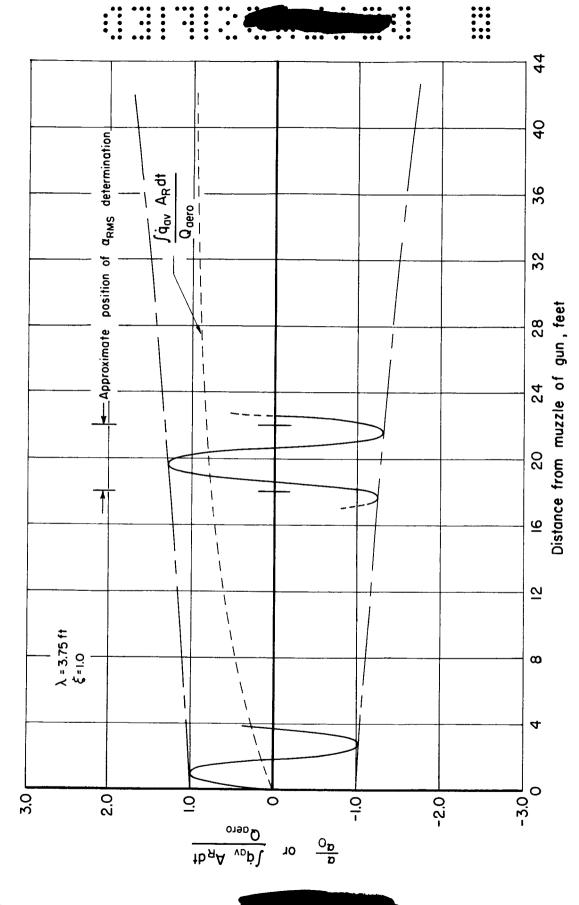
Figure 8.- Theoretical angle-of-attack history.
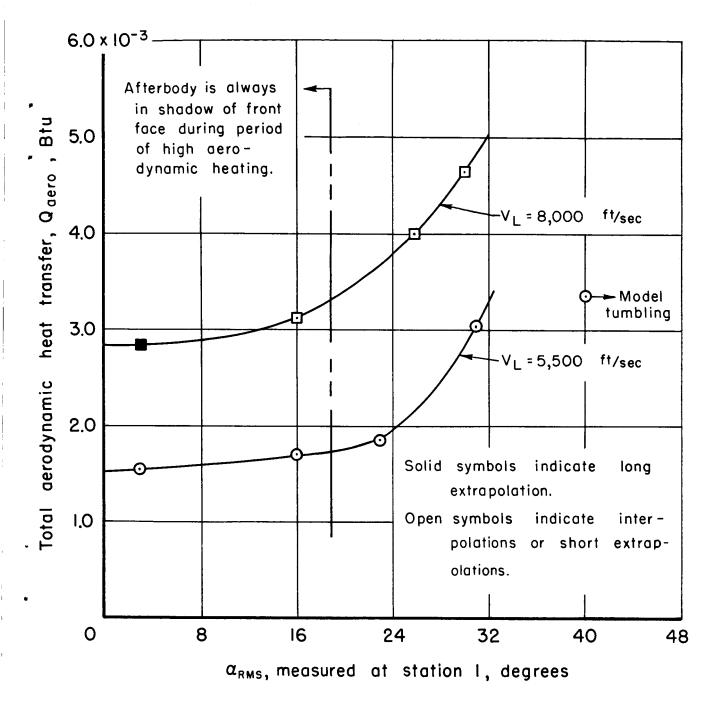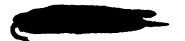
Figure 9.- Effect of RMS angle of attack on total aerodynamic heating of the blunt capsule.
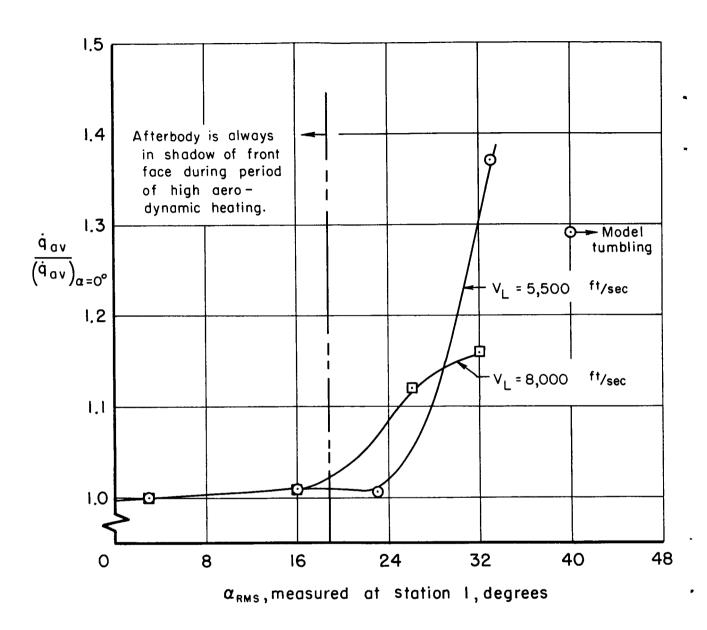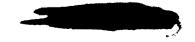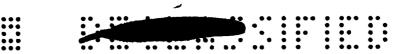
Figure 10.- Effect of RMS angle of attack on heat-transfer rates to the blunt capsule.
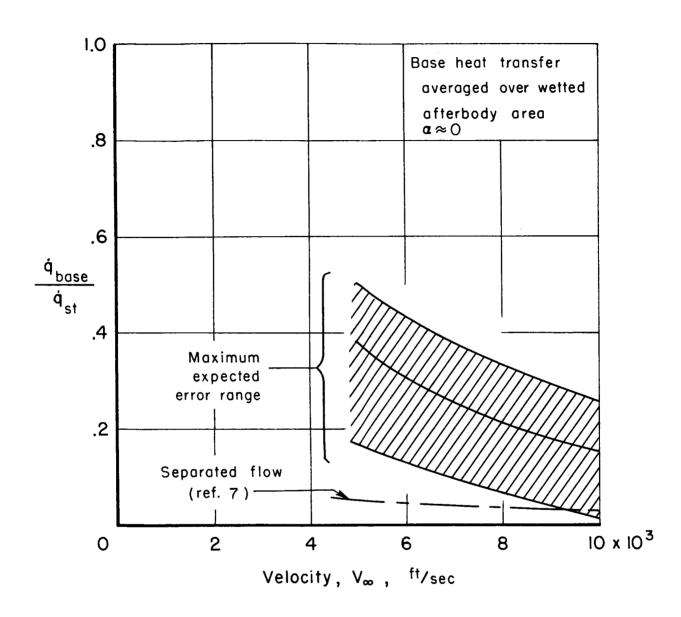
Figure 11.- Base heat transfer to the blunt capsule.
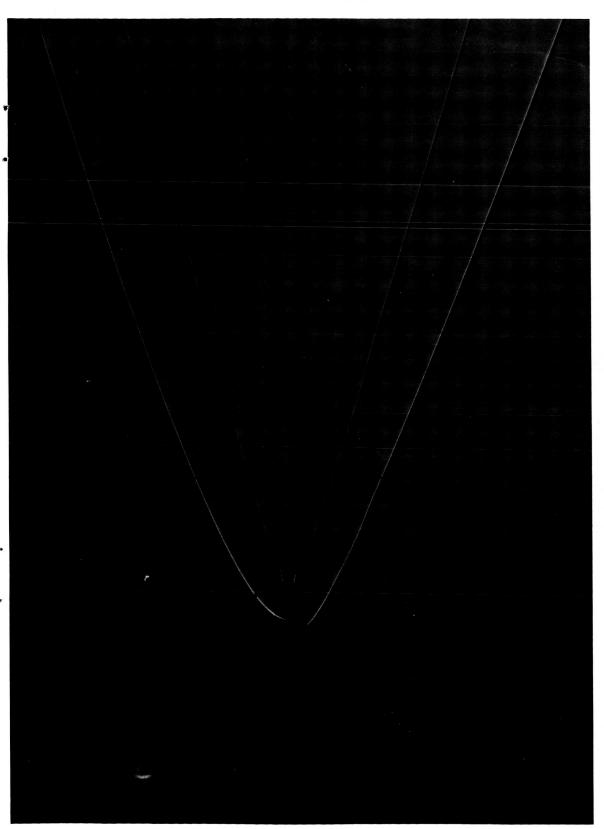
(a) $V_\infty = 3,370$ ft/sec, $R_\infty = 0.44$ million, $\alpha = -8.2^\circ$
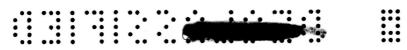
Figure 12.- Typical shadowgraphs of the blunt capsule at various angles of attack.
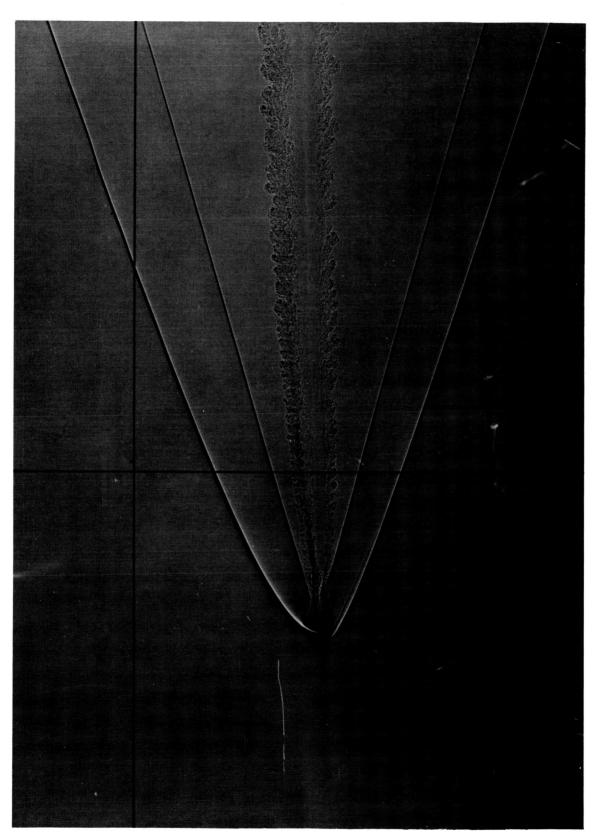
(b) V_∞ = 3,760 ft/sec, R_∞ = 0.49 million, α = 27.0°
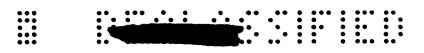
Figure 12.- Continued.

(c) $V_\infty = 3,800$ ft/sec, $R_\infty = 0.495$ million, $\alpha = 33.8°$

Figure 12.- Concluded.
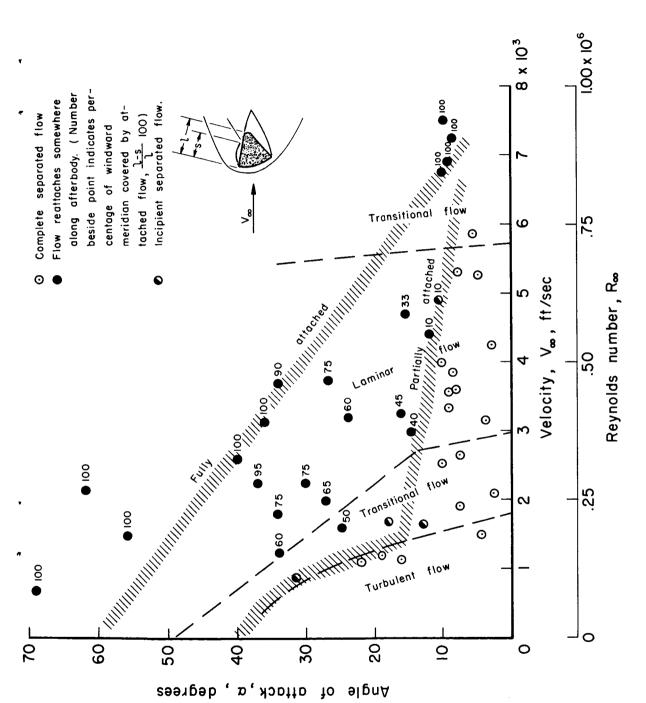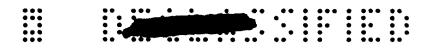
Figure 13.- Base flow on the windward side of the blunt capsule.
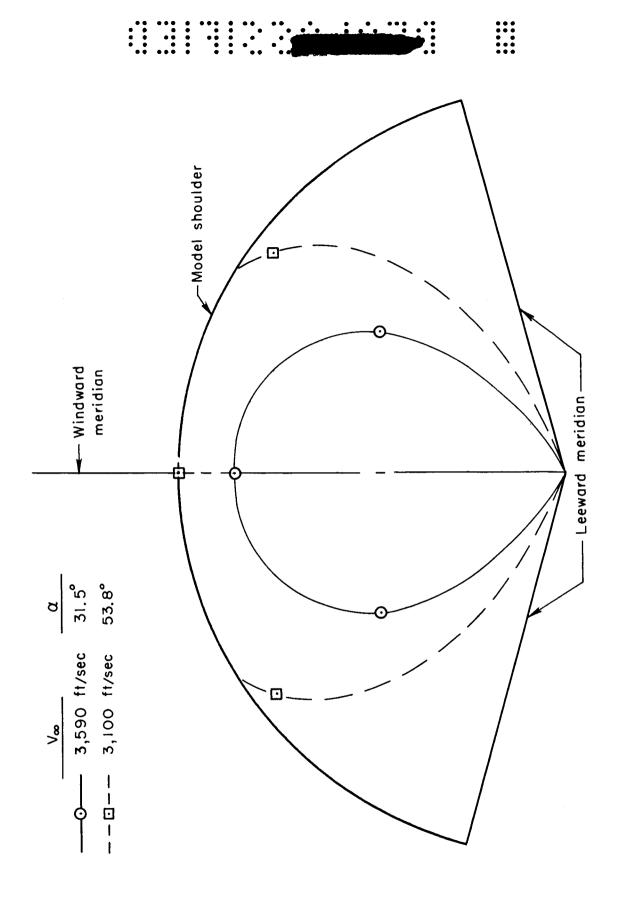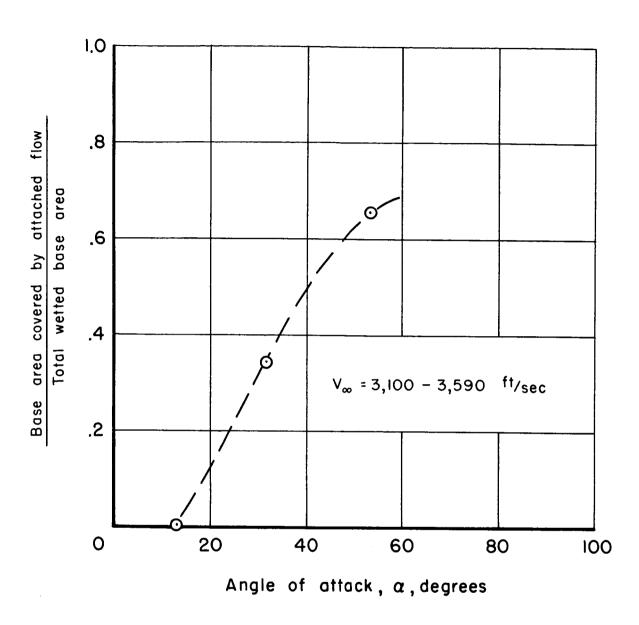
Figure 14.- Zones of attached flow.

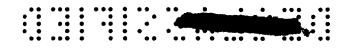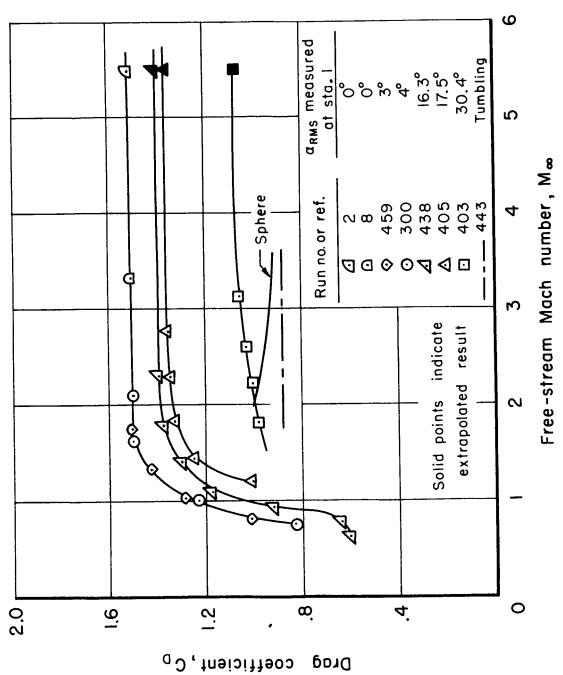Figure 15.- Fraction of the wetted base area covered by attached flow.

Figure 16.- Drag results of the blunt capsule.